Available online at www.sciencedirect.com
SCIENCE DIRECT®
International Journal of Heat and Mass Transfer 48 (2005) 609–620
International Journal of HEAT and MASS TRANSFER
www.elsevier.com/locate/ijhmt

Optimal geometry of L and C-shaped channels for maximum heat transfer rate in natural convection

A.K. da Silva [a,*], L. Gosselin [b]

[a] Department of Mechanical Engineering and Materials Science, Duke University, Box 90300, Durham, NC 27708-300, USA
[b] Département de génie mécanique, Université Laval, Québec, Canada G1K 7P4

Received 8 April 2004; received in revised form 6 August 2004
Available online 11 November 2004

Abstract

The present paper documents the geometric optimization of L and C-shaped channels in laminar natural convection subject to global constraints. The objective is to maximize the heat transfer rate from the hot wall to the coolant fluid. Three different configurations were considered: (i) an L-shaped asymmetric vertical heated channel with an adiabatic horizontal inlet, (ii) an asymmetric vertical heated channel with an adiabatic vertical outlet, and finally, (iii) a C-shaped vertical channel with horizontal inlet and outlet. The two first configurations are free to morph according to two degrees of freedom: the wall-to-wall spacing and inlet (or outlet) height. The third configuration is optimized with respect to the wall-to-wall spacing, and the heights of the inlet and outlet ports. The effect of the inlet or outlet horizontal adiabatic duct lengths is also investigated. The optimization is performed numerically by using the finite element technique, in the range $10^5 < Ra < 10^7$ for $Pr = 0.7$, where Ra is the Rayleigh number based on a fixed total height H of the channel. The numerical results show that optimization is relevant, since the three degrees of freedom considered have a strong effect on the heat transfer delivered from the hot wall to the fluid. The optimal geometric characteristics obtained numerically (i.e., optimal spacing, optimal height and lengths) are reported and correlated within a 7.5% maximal disagreement range.

Keywords: Natural convection; Maximum heat transfer rate; Optimal spacing; Vertical channel; Trombe wall; L-shaped channels

1. Introduction

The quest for better designs has always been a central goal in engineering. The necessity of constant improvement challenges scientists in most fields. In heat transfer, for example, the challenge could be translated as: how to heat, cool, serve, arrange for minimal cost or maximal performance?

Nowadays, with the increasing cheapness and availability of reliable numerical packages, optimization of convective flows (forced and natural) has become more popular. A review of the subject is given in Ref. [1], which focuses on the generation of shape and structure by maximizing global performance of flow systems subject to global constraints. This view is known as the constructal approach. One important branch of this theory concerns heat transfer augmentation, where dimensions reserved to fluids that act as a heating or cooling agent are optimized (e.g., enclosures, channels, staggered plates, fins).

* Corresponding author. Tel.: +1 919 660 5299; fax: +1 919 660 8963.
E-mail address: akd3@duke.edu (A.K. da Silva).

0017-9310/$ - see front matter © 2004 Elsevier Ltd. All rights reserved.
doi:10.1016/j.ijheatmasstransfer.2004.08.028

Nomenclature

c_P	specific heat, $\mathrm{J\,kg^{-1}\,K^{-1}}$
D	wall-to-wall spacing, m
g	gravity, $\mathrm{m\,s^{-2}}$
$\bar{h}$	average heat transfer coefficient, $\mathrm{W\,m^{-2}\,K^{-1}}$
H	height, m
H_{in}	inlet port height, m
H_{out}	outlet port height, m
k	thermal conductivity, $\mathrm{W\,m^{-1}\,K^{-1}}$
L	horizontal channel length, m
L_{d}	extended inflow length, m
L_{u}	extended outflow length, m
$\dot{m}'$	mass flow rate per unit of length, $\mathrm{kg\,s^{-1}\,m^{-1}}$
n	mesh trial
P	pressure, $\mathrm{N\,m^{-2}}$
Pr	Prandtl number
q'	heat transfer rate per unit of length, $\mathrm{W\,m^{-1}}$
$\bar{q}''_0$	average heat flux, $\mathrm{W\,m^{-2}}$
$\mathbf{R}$	residual vector
Ra	Rayleigh number, Eq. (10)
T_{w}	hot wall temperature, K
T_0	inlet fluid temperature, K
u	horizontal velocity component, $\mathrm{m\,s^{-1}}$
$\mathbf{u}$	solutions vector
v	vertical velocity component, $\mathrm{m\,s^{-1}}$
x, y	Cartesian coordinates, m
W	volume breadth, m

Greek symbols

α	thermal diffusivity, $\mathrm{m^2\,s^{-1}}$
β	coefficient of volumetric thermal expansion, $\mathrm{K^{-1}}$
ρ	density, $\mathrm{kg\,m^{-3}}$
σ	maximum error
ν	kinematic viscosity, $\mathrm{m^2\,s^{-1}}$
μ	viscosity, $\mathrm{N\,s\,m^{-2}}$

Subscripts

i	iteration index
n	mesh index

Superscript

$\sim$	dimensionless variables

In this paper, we take a closer look at a well-known class of heat transfer problems: the driven buoyancy flows. Due to its low cost, relative simplicity and reliability, natural convection has always been an attractive cooling technique in engineering. Its applications are countless, embracing different technical fields. For example, natural circulation powered by buoyancy forces in buildings and houses, also known as Trombe walls [2–8], are commonly used. Electronics can be thermally controlled by natural convection [9–20]. In nuclear and chemical reactors, buoyancy forces also play an important role.

In the present paper, we focus on a relatively new class of buoyancy driven flows, the L and C-shaped channels. Very few studies are available on the subject [21–23]. However, in none of them heat transfer augmentation under global constraints (optimization) was the main concern. This motivates the present paper in which we further investigate this class of channels. Our objective is to determine the optimal geometric features of the channel that maximize the total heat transfer rate from the hot wall to the coolant.

2. Optimally designed L-shaped channels

Consider the vertical asymmetrically heated channels shown in Fig. 1, where two different configurations are sketched: (a) a vertical channel with horizontal inlet and vertical outlet, shown in Fig. 1a, and (b) a vertical channel with a vertical inlet and a horizontal outlet, Fig. 1b. In each case, the temperature difference between the right-hand side hot wall and the cold fluid at the inlet triggers buoyancy forces. The fluid is driven upward, and by mass conservation, a suction effect is induced.

In both configurations, the total height H of the channel is fixed. In other words, H is the summation of the inlet (or outlet) port height, and heated section length. Each configuration is free to shape itself with respect to two degrees of freedom: (i) the wall-to-wall spacing D, and (ii), the inlet or outlet height, H_{in} or H_{out}. When H_{in} (or H_{out}) varies, the length of the heated section ($H - H_{\mathrm{in}}$) varies accordingly because of the constrained total height. H is the length scale used to nondimensionalize the degrees of freedom

$$(\widetilde{D}, \widetilde{H}_{\mathrm{in}}, \widetilde{H}_{\mathrm{out}}) = \frac{(D, H_{\mathrm{in}}, H_{\mathrm{out}})}{H} \tag{1}$$

The dimensionless total height is obviously equal to 1. The optimal L or C-shaped channel design refers to the geometrical features presented in Eq. (1) that maximizes the energy removed from the hot wall. Such figure of merit is based on the evaluation of the total energy transferred from the hot wall to the fluid (i.e. the heat transfer rate), and can be evaluated as follows:

$$q' = -k \int_0^H \left.\frac{\partial T}{\partial x}\right|_{x=D} \mathrm{d}y \tag{2}$$

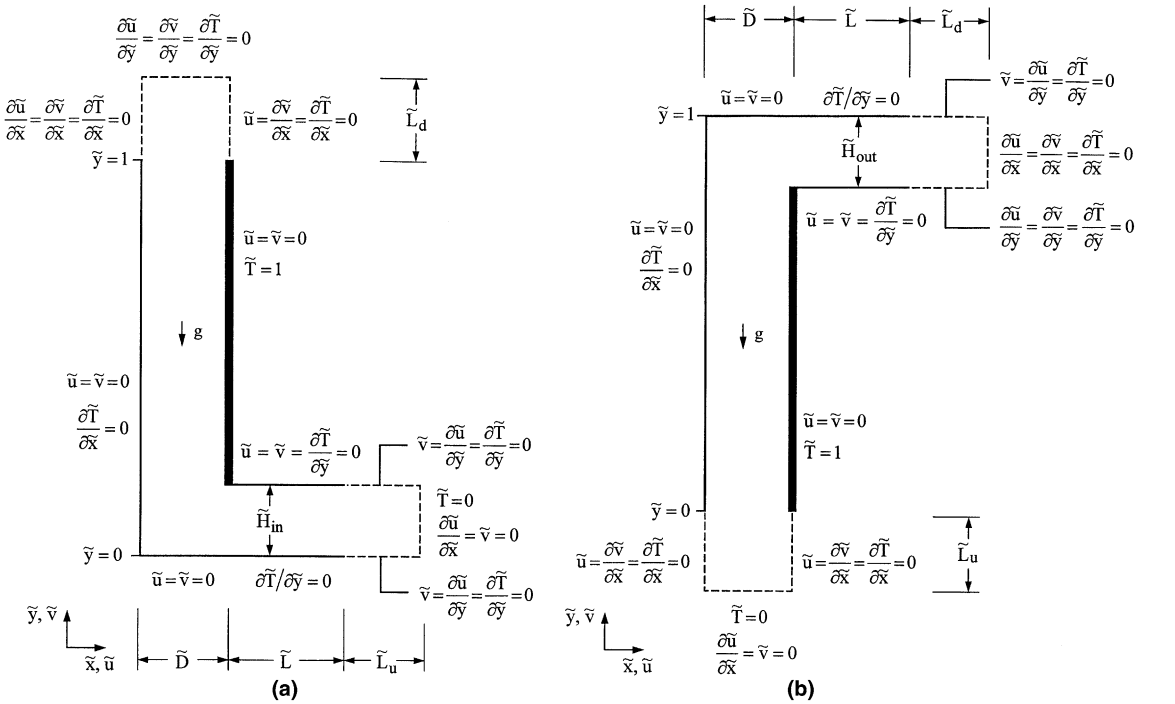

Fig. 1. The numerical domain and boundary conditions of a vertical heated channel with (a) a horizontal inlet, and (b) horizontal outlet.

where k is the thermal conductivity of the fluid. The heat transfer rate is written per unit length perpendicular to Fig. 1. Note that the evaluation of the heat transfer rate is performed from $y = H_{in}$ to $y = H$ for the setup shown in Fig. 1a, and from $y = 0$ to $y = H - H_{out}$ for the setup shown in Fig. 1b. The inlet or outlet ports occupy the remaining portion of the height H, and consequently, the energy added to the fluid in this region is zero. The dimensionless version of Eq. (2) reads as

$$\tilde{q}' = \frac{q'}{k(T_w - T_0)} \tag{3}$$

The existence of an optimal wall-to-wall spacing stems from the fact that when $\widetilde{D}$ is too small, the fluid reaches a temperature level equal to the one of the hot wall before the end of the wall. When this happens, the remaining heated length of the wall is not 'cooled' by the fluid, which reduces $\tilde{q}'$. In the other extreme when $\widetilde{D}$ is large, the fluid receives energy from the whole length of the hot wall, but the chimney effect, which accelerates the fluid upwards, is lost. This suggests the existence of an optimal wall-to-wall spacing $\widetilde{D}$ which maximizes $\tilde{q}'$.

The optimization of the inlet (or outlet) height is as important as the optimization of the wall-to-wall spacing. For a fixed H, the smaller the inlet and outlet ports, the larger the surface of exchange where heat can be removed by the fluid. However, in the limit where $\widetilde{H}_{in} \to 0$ or $\widetilde{H}_{out} \to 0$, the induced mass flow rate vanishes, and as a consequence, the heat transfer rate goes to zero, $\tilde{q}' \to 0$. This tradeoff suggests the existence of an optimum height for the inlet and outlet ports.

3. Intersection of asymptotes method

In this section we present scaling arguments to predict the optimal L-channel configuration in terms of heat transfer. At this point, we simplify the discussion by noting that the flow resistance is minimized when D and H_{in} (or H_{out}) are of the same order of magnitude [11]. In other words, avoiding abrupt changes in the cross-sectional area of the channel (i.e., $D \sim H_{in}$) leads to larger mass flow rate, and thus heat transfer rate. We also disregard the effect of the extension adiabatic length, L. The scale analysis is based on the case where $L \to 0$. When L is large, smaller heat transfer rates are to be expected due to friction losses in the extension that act as a brake diminishing the mass flow rate in the channel. In other words, the scale predictions of this section will overestimate the heat transfer rate when compared with a design where $L \neq 0$.

To determine the optimal port inlet height, we use the asymptote method [1,11,20]. The heat transfer rate scale is evaluated in two extreme limits ($H_{in} \to 0$ and $H_{in} \to H$). The optimal is approximately located where the curves corresponding to the two extreme limits intersect.

In the limit of small inlet port cross-section $H_{in} \to 0$ (and therefore $D \to 0$, according to the aforementioned assumption), the flow is fully developed in a large portion of the channel. One can use the solution obtained analytically for a fully developed flow between parallel plates in natural convection. For such configuration, the mass flow rate reads as [11]:

$$\dot{m}' \sim \frac{1}{2}\frac{\rho g \beta H_{in}^3 (T_w - T_0)}{12\nu} \tag{4}$$

The total heat transfer rate between the stream and the hot wall is

$$q'_{H_{in}\to 0} = \dot{m}' c_P (T_w - T_0) \tag{5}$$

i.e., by using Eq. (4),

$$q'_{H_{in}\to 0} = \frac{\rho g \beta c_P H_{in}^3 (T_w - T_0)^2}{24\nu} \tag{6}$$

Eq. (6) shows that in the fully developed limit q' scales as H_{in}^3.

In the other limit, $H_{in} \to H$, the heat current crosses a boundary layer that grows on the wall. The heat transfer rate can be determined by,

$$q'_{H_{in}\to H} = \bar{h}(T_w - T_0)(H - H_{in}) \tag{7}$$

For $Pr = 0.7$, the average heat transfer coefficient is [11]

$$\bar{h} = \frac{k}{(H - H_{in})} 0.516 \left[\frac{g\beta(T_w - T_0)(H - H_{in})^3}{\alpha\nu}\right]^{1/4} \tag{8}$$

By combining Eqs. (7) and (8), we obtain

$$q'_{H_{in}\to H} = 0.516 k (T_w - T_0) Ra^{1/4} (1 - H_{in}/H)^{3/4} \tag{9}$$

where Ra is the Rayleigh number defined as:

$$Ra = \frac{g\beta(T_w - T_0)H^3}{\alpha\nu} \tag{10}$$

In the large-H_{in} limit, the total transfer is proportional to $(1 - H_{in}/H)^{3/4}$.

The dimensionless version of the curves obtained in the two extreme limits, Eqs. (6) and (9), are reported in Fig. 2. The optimal inlet height can be approximated by the $\widetilde{H}_{in}$ value where the two curves intersect, $(q'_{\widetilde{H}_{in}\to 0})_{Eq.(6)} \cong (q'_{\widetilde{H}_{in}\to 1})_{Eq.(9)}$. The result in terms of the dimensionless variables introduced in Section 2 is

$$\frac{(1 - \widetilde{H}_{in,opt})}{\widetilde{H}_{in,opt}^4} \cong 0.03491\, Ra \tag{11}$$

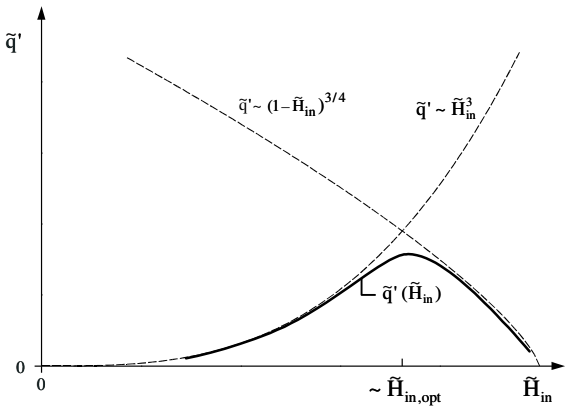

Fig. 2. The heat transfer rate in the limit of large ($\widetilde{H}_{in} \to 0$) and small ($\widetilde{H}_{in} \to 1$) inlet port and the asymptote method.

where Ra is the same as in Eq. (10). A particularly simple solution of Eq. (11) appears when $\widetilde{H}_{in} \ll 1$, in which case one can rewrite the nominator as $(1 - \widetilde{H}_{in,opt}) \sim (1 - 0.25\widetilde{H}_{in,opt})^4$. Eq. (11) then yields,

$$\widetilde{H}_{in,opt} \sim \frac{1}{0.25 + 0.43\, Ra^{1/4}} \tag{12}$$

It is worth mentioning that in an order of magnitude sense, the optimal outlet height (Fig. 1b) scales in the same way as the optimal inlet height (Fig. 1a) described above. Eq. (12) can be reintroduced in Eq. (6) or Eq. (9) to determine the maximum heat transfer rate, which now reads as

$$\tilde{q}'_{max} \sim 0.516\, Ra^{1/4}\left[1 - \frac{1}{0.25 + 0.43\, Ra^{1/4}}\right]^{3/4} \quad \text{for } Pr = 0.7 \tag{13}$$

As shown, the asymptote method and the scale analysis approach are a powerful tool that allows engineers and scientists to obtain quick estimates of optimal configurations. It is important though to understand the limits of the theoretical results that we obtained, Eqs. (12) and (13). In particular, the numerical factors in these equations provide us with an order of magnitude, not a precise value. For example, in Eq. (13), the factor 0.516 should be understood as a number of order 0.5. In fact, as we will see in Table 3, the numerical value is closer to 0.3, but in an order of magnitude sense, the two values are equivalent, as described is Refs. [1,11,20,26]. This should be kept in mind when evaluating the success of the scale analysis in comparison with numerical results, Sections 5 and 6. Another limit of the results presented in this section is that they have been derived in the limit $L \to 0$. When L is non-zero, the thermal performance will decrease. In other words, Eq. (13) overestimates the heat transfer rate when $L \neq 0$. The relative simplicity of the analysis presented in this section is certainly worth the approximate feature of Eq. (13).

4. Mathematical and numerical formulation

Consider the two-dimensional L-shaped channels shown in Fig. 1. For the vertical channel with a horizontal inlet, Fig. 1a, the numerical domain is composed of the extension of the inlet port ($L_u \times H_{in}$), the inlet port ($L \times H_{in}$), the main channel ($D \times H$), and the extension of the outlet domain ($D \times L_d$). For the channel with horizontal outlet, Fig. 1b, the numerical domain is composed of the extension of the inlet region ($D \times L_u$), the main vertical channel ($D \times H$), the outlet port ($L \times H_{out}$), and finally, the extension of the numerical outlet port ($L_d \times H_{out}$).

The mass flow rate and velocity profile at the entrance of the physical channel is unknown a priori: it depends on the geometry of the channel. The objective of inserting to the computational domain an 'artificial' extension to the inlet and outlet is for avoiding the inconvenience of having to specify any velocity or temperature profiles at the physical channel entrance or exit, by postponing the imposed velocity and temperature profiles to the inlet and outlet planes of the numerical extensions. The lengths L_u and L_d are long enough so that the flow can be considered fully developed in the extensions and in particular at the inlet and outlet planes of the numerical extensions. As we will see later, this simplifies the boundary conditions, with the drawback that the computational domain is larger than the physical domain. This approach has been used with success in [25,27], and in other fixed pressure drop problems [28].

Note that other approaches can be used to deal with the unknown velocity profile at the entrance [22]. In any case, it has been found that even though the velocity profile can be affected significantly by the choice of inlet boundary conditions, the heat transfer rate—the figure of merit considered in this paper—is relatively insensitive to the choice of boundary condition at the inlet [22]. In other words, in view of the scope of this paper, the decision to use extension domains rather than another numerical approach does not affect the optimization results.

The required lengths of the inlet and outlet extensions $\widetilde{L}_u = L_u/H$ and $\widetilde{L}_d = L_d/H$ were determined based on the variation of $\tilde{q}'$, Eq. (3), for each geometric configurations simulated. Tests showed that the solution becomes insensitive (i.e., the heat transfer rate changes by less than 0.5%) to any increment in the lengths of $\widetilde{L}_u$ and $\widetilde{L}_d$ when their values are approximately equal to 0.2. However, this insensitivity threshold value is slightly dependent on Ra. To avoid the inconvenience of changing $\widetilde{L}_u$ and $\widetilde{L}_d$ for every calculation, they have been set equal to 0.5—a number larger than 0.2—in all the simulations presented in this paper.

The conservation equations of mass, momentum and energy, for a single-phase two dimensional numerical domain were solved within the laminar range of $10^5 < Ra < 10^7$. To take into account the buoyancy force, the so-called Oberbeck–Boussinesq approach was used based on the assumption that the temperature difference between the hot wall and the cold fluid is small enough, $\beta(T_w - T_0) \ll 1$. This leads to the following dimensionless differential system:

$$\frac{\partial \tilde{u}}{\partial \tilde{x}} + \frac{\partial \tilde{v}}{\partial \tilde{y}} = 0 \tag{14}$$

$$\left(\frac{Ra}{Pr}\right)^{1/2}\left(\tilde{u}\frac{\partial \tilde{u}}{\partial \tilde{x}} + \tilde{v}\frac{\partial \tilde{u}}{\partial \tilde{y}}\right) = -\frac{\partial \widetilde{P}}{\partial \tilde{x}} + \nabla^2 \tilde{u} \tag{15}$$

$$\left(\frac{Ra}{Pr}\right)^{1/2}\left(\tilde{u}\frac{\partial \tilde{v}}{\partial \tilde{x}} + \tilde{v}\frac{\partial \tilde{v}}{\partial \tilde{y}}\right) = -\frac{\partial \widetilde{P}}{\partial \tilde{y}} + \nabla^2 \tilde{v} + \left(\frac{Ra}{Pr}\right)^{1/2}\widetilde{T} \tag{16}$$

$$(Ra\,Pr)^{1/2}\left(\tilde{u}\frac{\partial \widetilde{T}}{\partial \tilde{x}} + \tilde{v}\frac{\partial \widetilde{T}}{\partial \tilde{y}}\right) = \nabla^2 \widetilde{T} \tag{17}$$

where $\nabla^2 = \partial^2/\partial\tilde{x}^2 + \partial^2/\partial\tilde{y}^2$. The variables and the fluid properties are defined in the nomenclature. The governing equations were non-dimensionalized using the following variables

$$(\tilde{x}, \tilde{y}) = \frac{(x, y)}{H} \tag{18}$$

$$(\tilde{u}, \tilde{v}) = \frac{(u, v)}{(\alpha/H)\,Ra^{1/2}\,Pr^{1/2}} \tag{19}$$

$$\widetilde{T} = \frac{T - T_0}{T_w - T_0} \tag{20}$$

$$\widetilde{P} = \frac{P}{(\mu\alpha/H^2)\,Ra^{1/2}\,Pr^{1/2}} \tag{21}$$

where Ra is the Rayleigh number based on H, Eq. (10).

The boundary conditions are shown directly in Fig. 1. For all the surfaces represented by a solid line, the non-slip ($\tilde{u} = \tilde{v} = 0$) and impermeable boundary conditions were used. This includes the adiabatic vertical wall, inlet flow region of Fig. 1a, and outlet flow region of Fig. 1b. At the inlet of Fig. 1a—i.e. at the inlet of the extension, the vertical component of the velocity was assumed to be zero ($\tilde{v} = 0$). As a consequence, Eq. (14) yields $\partial\tilde{u}/\partial\tilde{x} = 0$, which represents a uniform velocity profile on that boundary. At the horizontal boundaries (side walls) of the inlet extension, free-slip and no penetration were assumed. In Fig. 1a, the u-component of the velocity was assumed to be zero (i.e. no penetration) in the right side of the vertical outlet extension, in addition to the free-slip. On the left side of the same numerical extension, free-slip with allowance of penetration was assured. Such consideration eliminates the unrealistic appearance of the chimney effect due to the extension of the numerical domain [25]. In the horizontal outlet plane $\partial\tilde{u}/\partial\tilde{y} = \partial\tilde{v}/\partial\tilde{y} = 0$ was specified.

In Fig. 1b, free-slip and no penetration were assumed in the vertical boundary of the inlet extensions. In the horizontal inlet boundary, a uniform velocity profile was specified as described above. In the outlet vertical plane, $\partial\tilde{u}/\partial\tilde{x} = \partial\tilde{v}/\partial\tilde{x} = 0$ were specified. The temperature of the hot wall and the inlet cold fluid were fixed equal to $\widetilde{T} = 1$ and $\widetilde{T} = 0$ respectively. All other surfaces of the numerical domain were considered adiabatic $\partial\widetilde{T}/\partial n = 0$, where n is the unit vector normal to the respective surface.

The numerical simulations were conducted using a commercial CFD package [24], which is based on the Galerkin finite elements method. The L-shaped numerical domain was discretized non-uniformly using quadrilateral elements with nine nodes each. For this type of element, the velocity and temperature are approximated using biquadratic interpolation functions. The discontinuous pressure approximations used was bilinear. When the value of a variable (e.g., velocity components and temperature) is specified at a boundary node, the particular discretized equation for that variable is disregarded, and the variable boundary value is used in the other equations. The fully coupled approach, which solves all conservation equations in a simultaneous coupled manner, was used. The explicit appearance of the pressure was eliminated based on a penalty function, with an error factor of 10^{-8}. The nonlinear equations resulting from the Galerkin finite element were solved by successive substitutions followed by the Newton–Raphson scheme. Such approach uses the slower but more robust character of the successive substitution method to bring the solution within the radius of convergence of the faster converging Newton methods. In order to control spatial numerical instabilities generated at high Ra, the upwind formulation was applied.

Two parameters were used for the determination of the convergence criteria: the solution vector $\mathbf{u}_i$ and the residual vector $\mathbf{R}(\mathbf{u}_i)$, where i is the iteration index. The convergence criteria for the solution vector is

$$\frac{\|\mathbf{u}_i - \mathbf{u}_{i-1}\|}{\|\mathbf{u}_i\|} \leqslant 0.001 \tag{22}$$

where $\|\cdot\|$ is the Euclidean norm. The use of the solution vector as a convergence criterion may mask the results accuracy. The reason for that stems from the fact that the difference between the solution vectors $\mathbf{u}_i - \mathbf{u}_{i-1}$ may be small because the step time between the two iterations is small, which can wrongly satisfy Eq. (22). A more reliable convergence criterion is based on the residual vector $\mathbf{R}(\mathbf{u}_i)$, which must tend to zero as $\mathbf{u}_i$ tends to the solution. This criterion reads as

$$\frac{\|\mathbf{R}(\mathbf{u}_i)\|}{\|\mathbf{R}_0\|} \leqslant 0.001 \tag{23}$$

where $\mathbf{R}_0$ is a reference vector, typically $\mathbf{R}(\mathbf{u}_0)$. The combination of Eqs. (22) and (23) provides an effective overall convergence criterion for all the problems studied in this paper, since both $\Delta\mathbf{u}_i = \mathbf{u}_i - \mathbf{u}_{i-1}$ and $\mathbf{R}(\mathbf{u}_i)$ tend to zero close to the solution.

Table 1
Grid refinement example, Fig. 1a

Mesh ($\tilde{x} \times \tilde{y}$)	Nodes	Elements	$\tilde{q}'$	$\left\|\frac{\tilde{q}'_n - \tilde{q}'_{n+1}}{\tilde{q}'_{n+1}}\right\|$
25×25	153	71	4.684857	–
51×51	525	200	4.868688	0.03775
75×75	1113	382	4.824711	0.00911
101×101	2321	720	4.940291	0.02339
151×151	4755	1399	5.017920	0.01547
201×201	8841	2490	5.068588	0.00999

Table 2
Grid refinement example, Fig. 1b

Mesh ($\tilde{x} \times \tilde{y}$)	Nodes	Elements	$\tilde{q}'$	$\left\|\frac{\tilde{q}'_n - \tilde{q}'_{n+1}}{\tilde{q}'_{n+1}}\right\|$
25×25	153	77	5.075517	–
51×51	705	257	5.161771	0.01671
75×75	1205	424	5.013852	0.02950
101×101	2441	775	5.040386	0.00526
151×151	4969	1491	5.085687	0.00890
201×201	9081	2600	5.120044	0.00671

The grid refinement tests showed that the ideal mesh is a function of the Rayleigh number. Furthermore, the mesh should be non-uniform in the $\tilde{x}$ direction, with the smaller elements located close to the verticals walls where intense velocity and temperature gradients are expected. The mesh accuracy study showed that for $Ra = 10^5$, 101 nodes per unit of length should be used in both directions. However, for $Ra_H = 10^6$ and 10^7, 201 nodes per unit of length were used in both directions. The mesh independence study is based on the figure of merit—the total heat transfer rate, Eq. (3). We require that the difference in terms of heat transfer rate be less than 1% for further doubling of the number of nodes.

Tables 1 and 2 show how grid independence was achieved in terms of dimensionless heat transfer rate for the L-shaped channel shown in Fig. 1a and b considering ($Ra = 10^5$, $Pr = 0.7$, $\widetilde{D} = 0.1$, $\widetilde{H}_{\text{in}} = 0.1$, $\widetilde{L} = 0.1$, and $\widetilde{L}_{\text{d}} = 0.5$) and ($Ra = 10^5$, $Pr = 0.7$, $\widetilde{D} = 0.1$, $\widetilde{H}_{\text{out}} = 0.1$, $\widetilde{L} = 0.1$, and $\widetilde{L}_u = 0.5$) respectively.

5. Numerical optimization of the L-shaped channel

The objective of the present paper is to optimize the geometry of the channel to maximize the total heat transfer rate, which is global parameter. Detailed velocity, temperature, and pressure fields within the channel

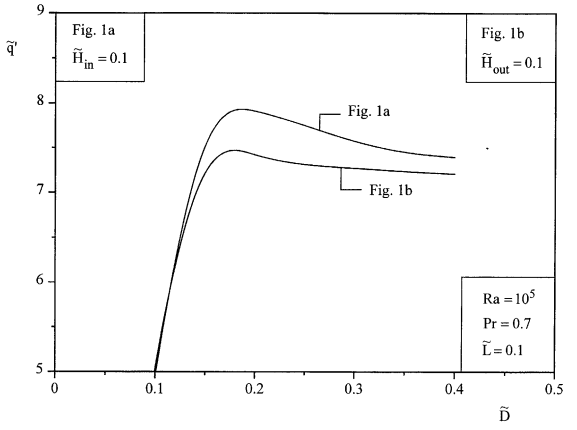

Fig. 3. The effect of the wall-to-wall spacing on the heat transfer rate of a L-shaped channel.

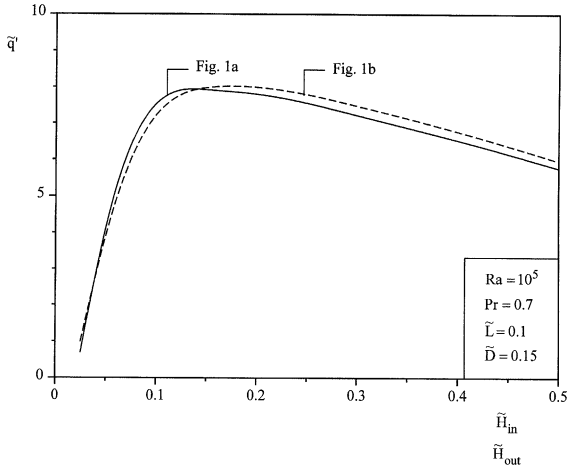

Fig. 4. The effect of the inlet and outlet height on the heat transfer rate.

can be found elsewhere [2–10,21,22], and therefore, we do no reproduce them here.

Fig. 3 shows that $\tilde{q}'$ can be optimized numerically with respect to the wall-to-wall spacing $\widetilde{D}$ for both configurations presented in Fig. 1, when $\widetilde{H}_{in}$ (or $\widetilde{H}_{out}$) is fixed. The maximum is relatively sharp for both configurations. However, the curves are not symmetric on each side of the maximum. According to Fig. 3, smaller values of the wall-to-wall spacing ($\widetilde{D} < \widetilde{D}_{opt}$) are much more detrimental to the thermal performance than the larger wall-to-wall spacing ($\widetilde{D} > \widetilde{D}_{opt}$) where the total heat transfer rate decreases slowly. The reason comes from the fact that, for small $\widetilde{D}$ values, the coolant fluid is overworked thermally. In other words, the fluid reaches a temperature equal to the temperature of the hot wall before the end of the channel heated section, which reduces tremendously the heat transfer rate.

The optimization opportunities in terms of inlet and outlet port heights ($\widetilde{H}_{in}$ or $\widetilde{H}_{out}$) are depicted in Fig. 4, for a fixed value of $\widetilde{D}$. Similarly to what was observed in Fig. 3, one notes that the behavior of the curve on each side of the maximum is different. Smaller than optimal values ($\widetilde{H}_{in,opt} < \widetilde{H}_{in}$ or $\widetilde{H}_{out,opt} < \widetilde{H}_{out}$) lead to smaller heat transfer rates than larger than optimal values.

The next step is to vary simultaneously $\widetilde{D}$ and $\widetilde{H}_{in}$ (or $\widetilde{H}_{out}$) to determine the geometry that maximizes the heat transfer rate. For the two configurations shown in Fig. 1, the optimization process was based on two similar nested loops. For Fig. 1a, fixed values of the Rayleigh number and of $\widetilde{L}$ were specified. The wall-to-wall spacing $\widetilde{D}$ is varied until the maximal heat transfer rate per unit of length is determined for a given $\widetilde{H}_{in}$. It is worth mentioning that the mesh was updated according to the variation of $\widetilde{D}$, by respecting the number of nodes per unit of dimensionless length described in Section 4. Once $\tilde{q}'$ was maximized with respect to $\widetilde{D}$, a slightly different value was specified for $\widetilde{H}_{in}$, and $\widetilde{D}$ was varied again in order to determine the new maximum value of $\tilde{q}'$. This process was repeated for three values of *Ra*, and three values of $\widetilde{L}$, until the set $\widetilde{D}_{opt}$ and $\widetilde{H}_{in,opt}$ that maximizes $\tilde{q}'$ is determined. This geometry corresponds to the optimal design. The same procedure was adopted for the configuration of Fig. 1b. However, in this case $\tilde{q}'$ was maximized with respect to $\widetilde{D}$ and $\widetilde{H}_{out}$.

Fig. 5 summarizes how the optimal wall-to-wall spacing responds to changes in $\widetilde{L}$ and *Ra* for both setups of Fig. 1: Fig. 1a (open symbols) and b (closed symbols). According to Fig. 5, the optimal spacing decreases as the Rayleigh number increases, regardless of the configuration or the length of the adiabatic horizontal sections $\widetilde{L}$. Another interesting aspect is the insensibility of $\widetilde{D}_{opt}$ with respect to the configuration (i.e., Fig. 1a or b), and length $\widetilde{L}$. This feature of $\widetilde{D}_{opt}$ allows us to express it as a function of the Rayleigh number only. Based on our numerical results, we find the following correlation:

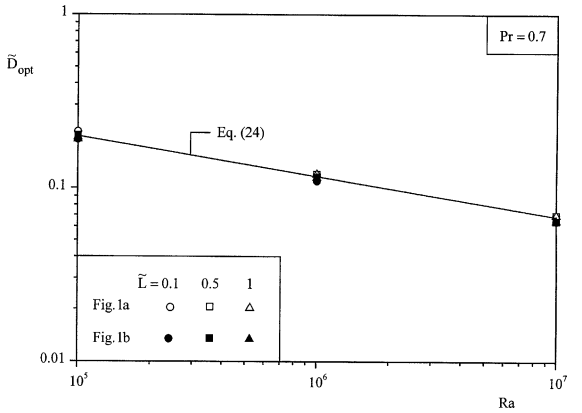

Fig. 5. The optimal wall-to-wall spacing of a vertical channel with horizontal inlets or outlets.

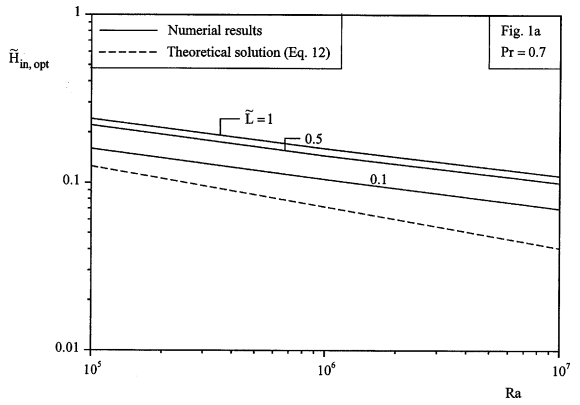

Fig. 6. The effect of adiabatic inlet horizontal length on the optimal inlet height.

$$\widetilde{D}_{opt} \cong 2.8\,Ra^{-0.23} \tag{24}$$

Eq. (24) is plotted in Fig. 5, and presents a maximum error of 5.6%.

Fig. 6 compares the optimal inlet height, $\widetilde{H}_{in,opt}$, obtained numerically with the analytical prediction of Section 3, Eq. (12), for the setup of Fig. 1a. It can be seen that the trend is the same for both solutions, and that the agreement becomes better as $\widetilde{L}$ goes to zero, which is the limit for which Eq. (12) has been derived. Another interesting aspect is that, according to the numerical results, $\widetilde{H}_{in,opt}$ is approximately proportional to $Ra^{-0.17}$, regardless of the horizontal length $\widetilde{L}$. Furthermore, for a fixed Rayleigh number, $\widetilde{H}_{in,opt}$ increases with $\widetilde{L}$. This means that the longer the walls of the inlet channel from which the cold fluid is drawn in, the larger the optimal mouth of this channel.

The same observations described above are valid for the optimal outlet height, $\widetilde{H}_{out,opt}$ as shown in Fig. 7. The optimal outlet port, $\widetilde{H}_{out,opt}$ scales as $\sim Ra^{-0.17}$, and increases with $\widetilde{L}$. The results presented in Figs. 5–7 confirm the assumption made in Section 3 that $\widetilde{D}_{opt}$, $\widetilde{H}_{out,opt}$, and $\widetilde{H}_{in,opt}$ have similar values. We note, though, that $\widetilde{H}_{out,opt}$ is approximately 14% larger than $\widetilde{H}_{in,opt}$ for the same values of Ra and $\widetilde{L}$.

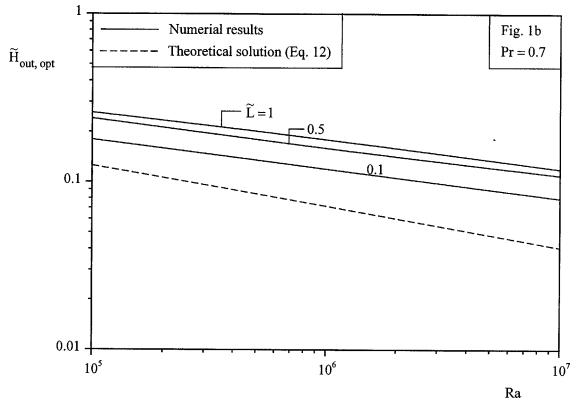

Fig. 7. The effect of adiabatic outlet horizontal length on the optimal outlet height.

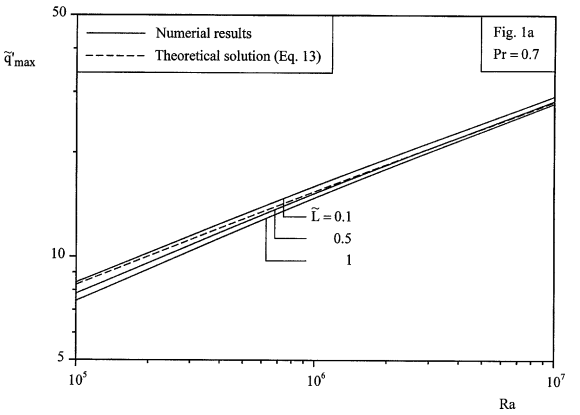

Fig. 8. The maximal heat transfer rate that corresponds to the optimized lengths reported in Figs. 6 and 7.

Fig. 8 shows the variation of maximum heat transfer rate, $\tilde{q}'_{max}$, for the configuration described in Fig. 1a as a function of $\widetilde{L}$ and Ra. From Fig. 8, it is clear that, for a fixed value of Ra, the maximum heat transfer rate decreases slightly as $\widetilde{L}$ increases, especially at low values of Ra. This is consistent with the idea that the mass flow rate decreases because of friction losses at the non-slip $\widetilde{L}$-channel walls. The longer the $\widetilde{L}$-walls, the more important the total friction losses. However, the numerical results show that for the range of $\widetilde{L}$-values considered, $\widetilde{L}$ has a minor effect on $\tilde{q}'_{max}$ in comparison with the other parameters.

For the sake of comparison, the scale prediction of Section 3 for the maximum heat transfer rate, Eq. (13), is plotted against the numerical results in Fig. 8.

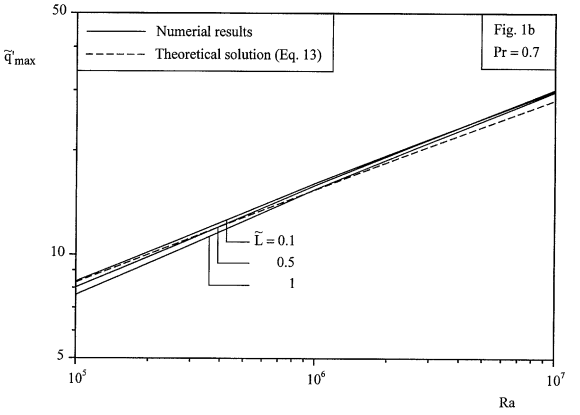

Fig. 9. The effect of the horizontal outlet length on the maximal heat transfer rate of a L-shaped channel of Fig. 1b.

The agreement between Eq. (13) and the numerical results can be considered good in an order of magnitude sense.

Fig. 9 shows the effect of $\widetilde{L}$ and Ra on the maximal heat transfer rate per unit of length for the configuration of Fig. 1b. Similarly to the behavior shown in Fig. 8, the performance of configuration Fig. 1b slightly decreases as $\widetilde{L}$ increases, especially at low values of Ra. Additionally, it is also shown that Eq. (13) agrees satisfactorily with the $\widetilde{q}'_{\max}$ results obtained numerically for Fig. 1b.

6. Numerical optimization of the C-shaped channel

The optimization procedure adopted for the C-shaped channel of Fig. 10 is similar to the one used in Fig. 1. However, in this case, three degrees of freedom are present: $\widetilde{D}$, $\widetilde{H}_{\text{in}}$, and $\widetilde{H}_{\text{out}}$. The optimal wall-to-wall spacing ($\widetilde{D}_{\text{opt}}$) is reported in Fig. 11 for different values of the horizontal extension and Rayleigh number. As in Fig. 5, $\widetilde{D}_{\text{opt}}$ decreases as Ra increases. For a fixed Ra number, no significant variation of $\widetilde{D}_{\text{opt}}$ was observed when varying $\widetilde{L}$. Based on the numerical results, the optimal spacing can be correlated as

$$\widetilde{D}_{\text{opt}} \cong 3.5\,Ra^{-0.25} \tag{25}$$

with a maximum error of 4.2%.

Fig. 12 shows the optimal inlet and outlet heights for the C-shaped channel of Fig. 10. It can be seen that both heights, $\widetilde{H}_{\text{in,opt}}$ and $\widetilde{H}_{\text{out,opt}}$, decrease as Ra increases. Also, for a fixed Ra number, $\widetilde{H}_{\text{in,opt}}$ and $\widetilde{H}_{\text{out,opt}}$ increase with $\widetilde{L}$. We stated in the previous sections that abrupt changes in the channel cross-section must be avoided to minimize the flow resistance (junction losses). This is verified by our results: $\widetilde{H}_{\text{in,opt}}$, $\widetilde{H}_{\text{out,opt}}$ and $\widetilde{D}_{\text{opt}}$ all have similar values. However, a new feature is revealed in Figs. 11 and 12. $\widetilde{H}_{\text{out,opt}}$ is slightly larger than $\widetilde{H}_{\text{in,opt}}$ (on average, 15% larger). For a large Rayleigh number ($Ra > 10^6$), we have $\widetilde{H}_{\text{in,opt}} < \widetilde{D}_{\text{opt}} < \widetilde{H}_{\text{out,opt}}$, i.e., that the optimal channel enlarges in the direction of the flow. This resembles a vertical divergent channel (i.e. that the intake width is narrower than the outlet width), which, according to [25], performs better than a straight vertical channel. The conclusion is that the optimal C-shaped

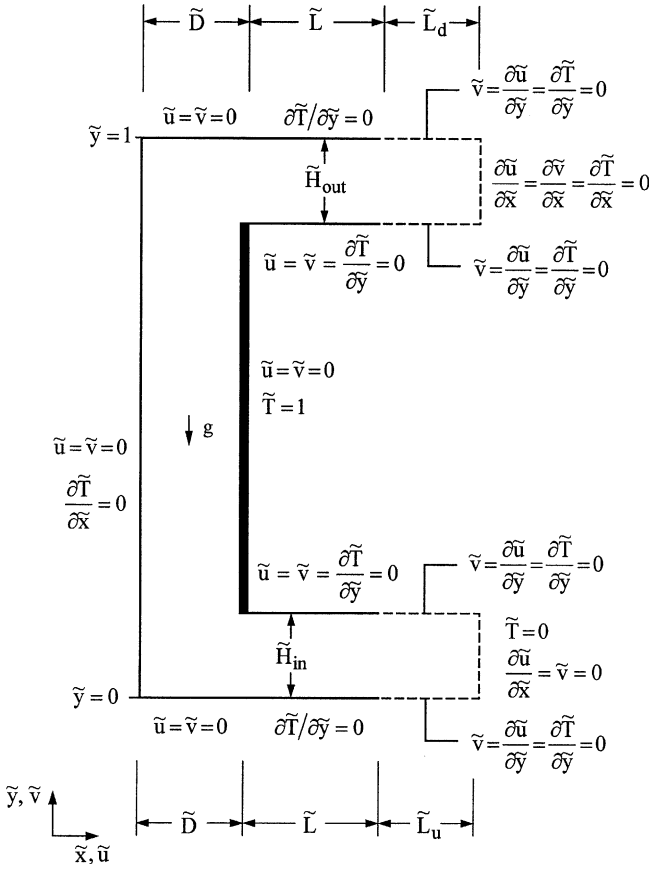

Fig. 10. The numerical domain and boundary conditions of a C-shaped channel.

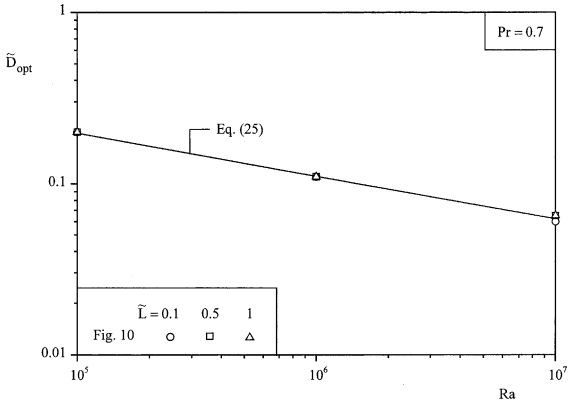

Fig. 11. The optimal wall-to-wall spacing of a C-shaped channel.

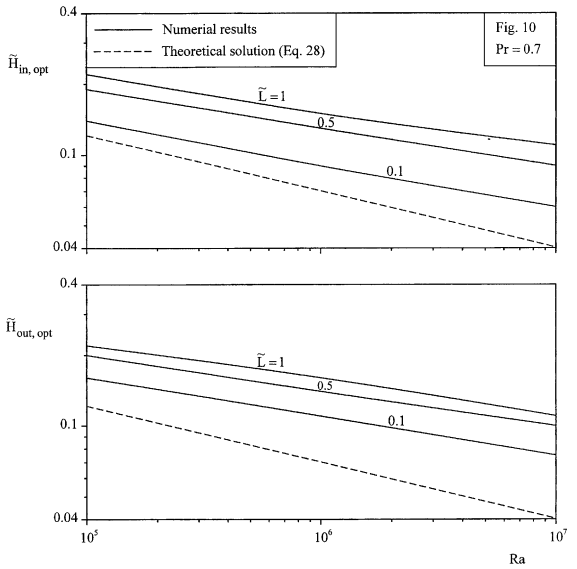

Fig. 12. The optimal inlet and outlet heights of a C-shaped channel.

configuration has a cross-section that increases slightly from one part of the channel to the other, but that these "changes" in terms of channel cross-section are small and smooth.

The order of magnitude analysis performed for the L-shaped channels described in Section 3, can be adapted to the present case by assuming that abrupt changes between parallel walls are once more avoided in the optimal configuration (i.e. $\widetilde{D}_{\mathrm{opt}} \sim \widetilde{H}_{\mathrm{in,opt}} \sim \widetilde{H}_{\mathrm{in,opt}}$). By relying on this assumption, one can observe that Eq. (6) still holds for the C-shaped channel. However, Eq. (9) now reads as

$$\frac{q'_{\widetilde{H}_{\mathrm{in}}\to 0.5}}{k(T_{\mathrm{w}}-T_0)} = 0.516\,Ra^{1/4}(1-2\widetilde{H}_{\mathrm{in}})^{3/4} \tag{26}$$

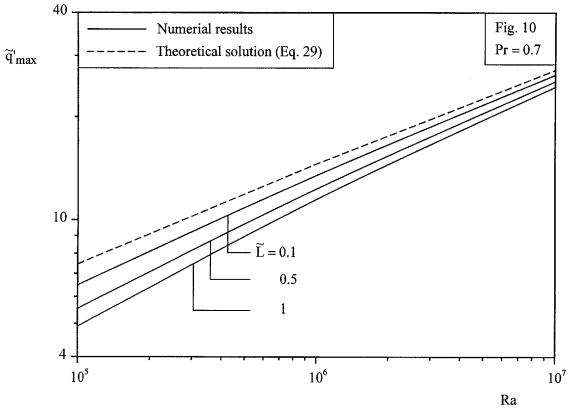

Fig. 13. The maximal heat transfer rate of a C-shaped channel that corresponds to the optimized lengths reported in Figs. 11 and 12.

and consequently the optimal inlet and outlet heights of the C-shaped channels scale as

$$\frac{(1-2\widetilde{H}_{\mathrm{in,opt}})}{\widetilde{H}^4_{\mathrm{in,opt}}} \cong 0.03491\,\mathrm{Ra} \tag{27}$$

By using the same simplification as in Section 3, we can also rewrite Eq. (27) as

$$\widetilde{H}_{\mathrm{in,opt}} \sim \frac{1}{0.5+0.432\,Ra^{1/4}} \tag{28}$$

Reintroducing Eq. (28) in Eq. (26) leads to a maximum heat transfer rate of

$$\tilde{q}'_{\max} = 0.516\,Ra^{1/4}\left[1-\frac{1}{0.25+0.216\,Ra^{1/4}}\right]^{3/4} \quad \text{for } Pr = 0.7 \tag{29}$$

Eq. (27) is plotted against the numerical results in Fig. 12 with a relatively good agreement, especially in the upper frame, which reports $\widetilde{H}_{\mathrm{in,opt}}$.

Finally, Fig. 13 shows the effect of $\widetilde{L}$ and Ra on $\tilde{q}'_{\max}$ for the channel sketched in Fig. 10. As expected, the maximum heat transfer rate decreases as $\tilde{L}$ increases. Furthermore, we note that maximum heat transfer rates achieved with the C-channel are always smaller than the ones obtained with the L-channels. Eq. (29) is reported in Fig. 13. The numerical results agree reasonably with the scaling prediction when $Ra \sim 10^7$.

7. Conclusions

In this paper, we showed numerically and theoretically that the heat transfer rate per unit of length can

Table 3
Numerical optimal parameters and maximum heat transfer rate for the three channels studied in this paper

	$\widetilde{D}_{opt}$	(σ_{max} <)	$\widetilde{H}_{in,opt}$	(σ_{max} <)	$\widetilde{H}_{out,opt}$	(σ_{max} <)	$\tilde{q}'_{max}$	(σ_{max} <)
Fig. 1a	$2.8\,Ra^{-0.23}$	(5.6%)	$1.7\widetilde{L}^{0.18}\,Ra^{-0.17}$	(3.6%)	–		$0.265\widetilde{L}^{-0.05}\,Ra^{0.29}$	(7.5%)
Fig. 1b	$2.8\,Ra^{-0.23}$	(4.3%)	–		$1.85\widetilde{L}^{0.16}\,Ra^{-0.17}$	(8.2%)	$0.28\widetilde{L}^{-0.02}\,Ra^{0.29}$	(5.5%)
Fig. 10	$3.5\,Ra^{-0.25}$	(4.2%)	$1.6\widetilde{L}^{0.22}\,Ra^{-0.17}$	(6%)	$1.45\widetilde{L}^{0.17}\,Ra^{-0.16}$	(6.2%)	$0.09\widetilde{L}^{-0.08}\,Ra^{0.35}$	(5.5%)

be maximized by optimizing the wall-to-wall spacing $\widetilde{D}$, and the heights of the inlet and outlet ports of L and C-shaped channels in laminar natural convection. The global constraint used during the optimization is the total height of the channel. The numerical simulations, which were conducted in the range $10^5 < Ra < 10^7$, showed that the optimal spacings ($\widetilde{D}_{opt}$) decrease as Ra increases, and that they are insensible to adiabatic extension length $\widetilde{L}$ for the three configurations considered, Fig. 1a, b and Fig. 10. On the other hand, $\widetilde{H}_{in,opt}$ and $\widetilde{H}_{out,opt}$ depend on $\widetilde{L}$ and on the configuration selected. Another important conclusion is that an optimized configuration of the L-shaped channel performs better than optimized C-shaped channels (i.e., $\tilde{q}'_{max,\ Fig.1} > \tilde{q}'_{max,\ Fig.11}$). The correlation obtained numerically for the optimal parameters ($\widetilde{D}_{opt}$, $\widetilde{H}_{in,opt}$ and $\widetilde{H}_{out,opt}$) and maximum heat transfer rate are reported in Table 3, for the different configurations studied in this paper.

Acknowledgment

A.K. da Silva's work was fully supported by the Brazilian Research Council—CNPq (Conselho Nacional de Desenvolvimento Científico e Tecnológico), Brazil.

References

[1] A. Bejan, Shape and Structure, from Engineering to Nature, Cambridge University Press, Cambridge, UK, 2000.
[2] A.V. Sebald, J.R. Clinton, F. Langenbacker, Performance effects of trombe control strategies, Solar Energy 23 (1979) 479–487.
[3] H. Akbari, T.R. Borgers, Free convective laminar flow within the trombe wall channel, Solar Energy 22 (1979) 165–174.
[4] A. Akbarzadeh, W.W.S. Charters, D.A. Lesslie, Thermocirculation characteristics of a trombe wall passive test cell, Solar Energy 28 (1982) 461–468.
[5] S.J. Ormiston, G.D. Raithby, K.G.T. Hollands, Numerical predictions of natural convection in a trombe wall system, Int. J. Heat Mass Transfer 29 (1986) 869–877.
[6] R. Ben Yedder, E. Bilgen, Natural convection and conduction in trombe wall systems, Int. J. Heat Mass Transfer 34 (1991) 1237–1248.
[7] G. Gan, A parametric study of Trombe walls for passive cooling of buildings, Energy Bldg. 27 (1998) 37–43.
[8] A.M. Rodrigues, A. Canha da Piedade, A. Lahellec, J.Y. Grandpeix, Modeling natural convection in a heated vertical channel for room ventilation, Bldg. Environ. 35 (2000) 455–469.
[9] W. Aung, Fully developed laminar free convection between vertical plates heated asymmetrically, Int. J. Heat Mass Transfer 15 (1972) 1577–1580.
[10] W. Aung, L.S. Fletcher, V. Sernas, Developing laminar free convection between vertical plates with asymmetric heating, Int. J. Heat Mass Transfer 15 (1972) 2293–2308.
[11] A. Bejan, Convection Heat Transfer, third ed., Wiley, New York, 2004, p. 225.
[12] A. Bar-Cohen, W.M. Rohsenow, Thermally optimum spacing of vertical, natural convection cooled, parallel plates, J. Heat Transfer 116 (1984) 116–123.
[13] J.R. Leith, Thermal design considerations in vertical-channel with natural-convection, J. Heat Transfer 109 (1987) 249–251.
[14] N.K. Anand, S.H. Kim, L.S. Fletcher, The effect of plate spacing on free-convection between heated parallel plates, J. Heat Transfer 114 (1992) 515–518.
[15] A.G. Straarman, J.D. Tarasuk, J.M. Floryan, Heat transfer enhancement from a vertical, isothermal channel generated by chimney effect, J. Heat Transfer 115 (1993) 395–402.
[16] L.E. Howle, A comparison of the reduced Galerkin and pseudo-spectral methods for simulation of steady Rayleigh–Bénard convection, Int. J. Heat Mass Transfer 39 (1996) 2401–2407.
[17] L.E. Howle, The effect of boundary properties on controlled Rayleigh–Bénard convection, J. Fluid Mech. 411 (2000) 39–58.
[18] S. Kazansky, V. Dubovsky, G. Ziskind, R. Letan, Chimney-enhanced natural convection from a vertical plate: experiments and numerical simulations, Int. J. Heat Mass Transfer 46 (2003) 497–512.
[19] A. Auletta, O. Manca, M. Musto, S. Nardini, Thermal design of symmetrically and asymmetrically heated channel-chimney systems in natural convection, Appl. Thermal Eng. 23 (2003) 605–621.
[20] A. Bejan, Optimal internal structure of volumes cooled by single-phase forced and natural convection, J. Electron. Packaging 125 (2003) 200–207.
[21] G. Gan, S.B. Riffat, A numerical study of solar chimney for natural ventilation of buildings with heat recovery, Appl. Thermal Eng. 18 (1998) 1171–1187.
[22] F. Marcondes, C.R. Maliska, Treatment of the inlet boundary conditions in natural-convection in open-ended channels, Numer. Heat Transfer Part—B 35 (1999) 317–345.
[23] C.R. Maliska, Computational Heat Transfer and Fluid Dynamics, Rio de Janeiro, RJ, LTC—Livros Técnicos e Científicos, S.A., 1995.

[24] FIDAP Manual, Fluid Dynamics International, Inc. 1998.
[25] A.K. da Silva, A. Bejan, S. Lorente, Maximal heat transfer density in vertical morphing channels with natural convection, Numer. Heat Transfer Part—A 45 (2004) 135–152.
[26] L. Gosselin, M. Lacroix, Heat transfer and banks formation in a slag bath with embedded heat sources, Int. J. Heat Mass Transfer 46 (2003) 2537–2545.
[27] B. Biagio Morrone, A. Campo, O. Manca, Optimum plate separation in vertical parallel-plate channels for natural convective flows: incorporation of large spaces at the channel extremes, Int. J. Heat Mass Transfer 40 (1997) 993–1000.
[28] T. Bello-Ochende, A. Bejan, Fitting the duct to the "body" of convective flow, Int. J. Heat Mass Transfer 46 (2003) 1693–1701.